Robust gapped surface states and filtering effect in a photonic topological gyroelectromagnetic metamaterial

Ning Han,[1] Jianlong Liu,[2,*] Yang Gao,[3] Keya Zhou,[1] and Shutian Liu[1,†]

[1]*School of Physics, Harbin Institute of Technology, Harbin 150001, China*

[2]*Key Laboratory of In-Fiber Integrated Optics of Ministry of Education, College of Physics and Optoelectronic Engineering, Harbin Engineering University, Harbin 150001, China*

[3]*College of Electronic Engineering, Heilongjiang University, Harbin 150080, China*

(Received 2 August 2021; revised 22 October 2021; accepted 26 October 2021; published 1 November 2021)

The recent reported robust surface states in a photonic metamaterial are usually limited to the gapless type. In this work, we propose a photonic topological metamaterial that can support surface states with gaps. The gaps appear when the electromagnetic duality symmetry of the material system is broken. Despite the existence of gaps, the surface waves can still bypass sharp corners robustly. We further demonstrate the filtering effect which can be viewed as a fingerprint of the existence of the gapped surface states. By changing the electromagnetic parameters of the covering materials, the filtering effect with controllable bandwidth can be realized.

DOI: 10.1103/PhysRevB.104.205403

I. INTRODUCTION

In the past decade, topological photonics has emerged as a rapidly developing research field [1–3]. It opens up an intriguing way to control the propagation of electromagnetic waves. Various photonic topological phases have been proposed and realized, including topological insulators [4], higher-order topological states [5], and topological semimetals [6]. They have enriched opportunities for realizing singular topological models and exploring and utilizing topological effects in new ways. In particular, topological insulators have the characteristics of bulk insulation but edge/surface conduction [1]. The key feature of edge/surface states is that they can remain robust against defects and overcome backscattering [7–16].

Recently, the robust transport property of the gapped edge states has been proved in photonic crystals [17–21]. For example, in a photonic crystal system, when the C_6 symmetry is broken at the interface, a gap is opened near the point Γ and the gapped edge states emerge [21]. Because of the appearance of bandgaps, a direct question to ask is whether filtering effect exists in a photonic topological system with the gapped edge states. To the best of our knowledge, the filtering effect research in topological materials is still limited to the electronic systems [22–27]. In particular, the spin filtering effect in topological Dirac semimetals [24] and the valley filtering effect in a topological domain wall [26] have been proposed and studied recently.

The electromagnetic metamaterials provide a new method to produce photonic surface modes [13–16]. For example, the triple degenerate points and the bulk-edge correspondence in hyperbolic metamaterials have been studied [15]. The gyroelectromagnetic metamaterial is a new-type artificial medium [28–33]. It simultaneously has nonzero gyrotropic elements in the permeability and permittivity tensors. The gyroelectromagnetic metamaterials have been extensively studied in the fields of topological transitions [28], extraordinary dispersion [29], symmetry-protected scattering anomaly [30], and highly localized surface waves [33]. However, to the best of our knowledge, the gapped surface states have not been studied in the metamaterial system. Hence, two important questions naturally arise. Can the robust gapped photonic surface states exist in the gyroelectromagnetic metamaterial system? If so, can the filtering effect be realized based on the gapped surface states in the photonic topological metamaterial system?

In this work, the robust gapped surface states are demonstrated and we propose to use them to realize optical filtering effect for the surface waves on the photonic gyroelectromagnetic metamaterial. In particular, the gapped surface states arise when the electromagnetic duality symmetry of the material system is broken. We demonstrate that the surface states can still propagate stably around sharp corners. The filtering effect emerges concomitantly in the gapped surface states. The mechanism of the filtering effect is that the surface waves with the same polarization can nearly freely pass through, but those in the gap are totally blocked. The filtering effect with controllable bandwidth can be realized by changing the electromagnetic parameters of the covering materials.

The paper is organized as follows. In Sec. II, the band structures of the gyroelectromagnetic metamaterial are given. In Sec. III, the topological invariants and photonic surface states on the metamaterial are investigated. The gapless photonic surface waves on the metamaterial are given in Sec. IV. Gapped photonic surface states and robust surface waves are shown in Sec. V. Filtering effect in the photonic topological gyroelectromagnetic metamaterial system is given in Sec. VI. In Sec. VII, the realization of the gyroelectromagnetic metamaterial is proposed. The conclusions are given in Sec. VIII.

*liujl@hrbeu.edu.cn
†stliu@hit.edu.cn

II. BAND STRUCTURES

The permittivity tensor of the uniaxial anisotropic gyroelectromagnetic metamaterial is

$$\bar{\boldsymbol{\epsilon}} = \begin{pmatrix} \epsilon_t & ig & 0 \\ -ig & \epsilon_t & 0 \\ 0 & 0 & \epsilon_z \end{pmatrix}. \tag{1}$$

Here, g represents gyrotropic effect which is determined by the applied magnetic field along the z direction. It means the time-reversal symmetry of the metamaterial is broken. We assume that the gyroelectromagnetic metamaterials have electromagnetic duality symmetry, i.e., $\bar{\boldsymbol{\mu}} = \bar{\boldsymbol{\epsilon}}$. The electromagnetic duality is a natural property in free space [34]. The electromagnetic duality model has been applied in many works in recent years [35–44]. For example, the electromagnetic duality symmetry is utilized to realize the photonic Dirac points [35], spin-locked edge states in the photonic crystals [40], and three-dimensional photonic topological insulators [44].

The band structures of the nondispersion gyroelectromagnetic metamaterials can be obtained by solving the Maxwell's equations. The Maxwell's equations can be transformed into an eigenfrequency form $\hat{H}|\boldsymbol{\Psi}\rangle = \omega|\boldsymbol{\Psi}\rangle$ [15,45], with eigenfrequency ω, operator $\hat{H}$, and eigenvector $|\boldsymbol{\Psi}\rangle$:

$$\hat{H} = \begin{pmatrix} \bar{\boldsymbol{\epsilon}} & 0 \\ 0 & \bar{\boldsymbol{\mu}} \end{pmatrix}^{-1} \begin{pmatrix} 0 & \bar{\boldsymbol{\kappa}} \\ -\bar{\boldsymbol{\kappa}} & 0 \end{pmatrix}, \quad |\boldsymbol{\Psi}\rangle = \begin{pmatrix} \mathbf{E} \\ \mathbf{H} \end{pmatrix}, \tag{2}$$

where $\bar{\boldsymbol{\kappa}}$ is the skew-symmetric tensor of wave vector $\mathbf{k}$. In the present study, the wave vector is normalized to k_0, where k_0 is the wave number in vacuum. The eigenfrequency is normalized to ck_0, where c represents the speed of light in vacuum. Note that the state at $(\mathbf{k}, \omega)$ stands for the same physical state at $(-\mathbf{k}, -\omega)$ owing to the symmetry $\hat{H}(-\bar{\boldsymbol{\kappa}}) = -\hat{H}(\bar{\boldsymbol{\kappa}})$ [15]. Therefore, for better visualization, we only consider the part of the band structures with $\omega > 0$.

The band structures for different electromagnetic parameters are plotted in Fig. 1. Starting with an isotropic medium with $\epsilon_t = \epsilon_z = 2$ and $g = 0$, at this time the bulk state of the medium is hyperbolic, as illustrated in Fig. 1(a). When the gyrotropic parameter g is not zero (e.g., $g = 0.5$), the two bulk modes with different polarizations are lifted, as shown in Fig. 1(b). However, there is no common bandgap between the bulk states and the vacuum state. On the other hand, when ϵ_z is tuned to a negative value while keeping ϵ_t fixed, as illustrated in Fig. 1(c), the double semi-ellipsoid-like bands are well separated from the vacuum. The common bandgap [gray region in Fig. 1(c)] is a prerequisite for the formation of photonic surface states. Moreover, there is a degenerate line between the metamaterial and vacuum state when $g > (\sqrt{\epsilon_z}\sqrt{\epsilon_z + 4\epsilon_t^2\epsilon_z + 4\sqrt{\epsilon_t^2\epsilon_z^2}} - \epsilon_z)/2\epsilon_z (g > 1)$, as shown in Fig. 1(d). In this case, there is also no common bandgap between the semi-ellipsoid-like band and vacuum. In the following work, we will study and discuss the topological properties of the metamaterial in Fig. 1(c).

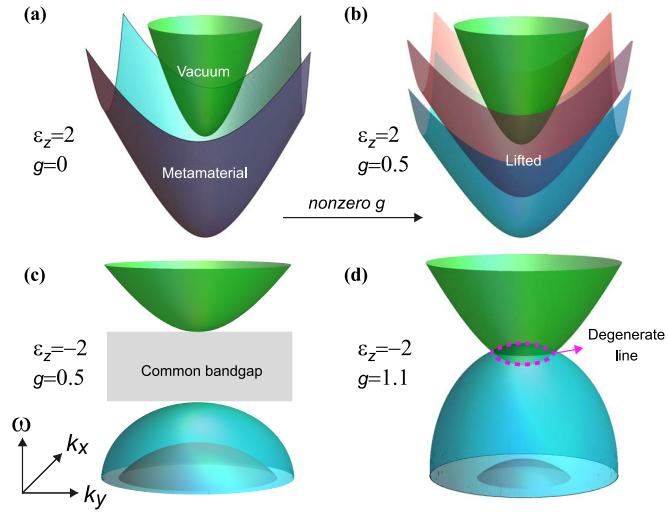

FIG. 1. Evolution of band structures due to changing the material parameters. (a) Isotropic medium with $g = 0$ and $\epsilon_z = 2$. (b) The double hyperbolic gyroelectromagnetic metamaterial with $g = 0.5$ and $\epsilon_z = 2$. (c) and (d) The double semi-ellipsoid-like gyroelectromagnetic metamaterial with $g = 0.5/g = 1.1$ and $\epsilon_z = -2$, respectively. The magenta dotted line represents the degeneracy between the metamaterial and vacuum state. Here, the green bands are the vacuum state. The other parameters are $\epsilon_t = 2$ and $k_z = 1$ for all plots.

III. TOPOLOGICAL INVARIANTS AND PHOTONIC SURFACE STATES

The characteristics of the band structures in the gyroelectromagnetic metamaterial can be characterized by the topological invariants (Berry phase/Chern numbers). In mathematics, the Berry phase can be expressed as the integral of Berry curvature. The Berry phase of the eigenmode in optical media is expressed [1],

$$\gamma = i \oint \nabla_{\mathbf{k}} \times \langle \mathbf{U}(\mathbf{k}) | \nabla_{\mathbf{k}} | \mathbf{U}(\mathbf{k}) \rangle \cdot d\mathbf{k}, \tag{3}$$

where $\mathbf{U}(\mathbf{k}) = [\mathbf{E}, \mathbf{H}]^T$ represents an eigenpolarization state of the media and $\Omega = \nabla_{\mathbf{k}} \times \langle \mathbf{U}(\mathbf{k}) | \nabla_{\mathbf{k}} | \mathbf{U}(\mathbf{k}) \rangle$ is the Berry curvature. Moreover, the Chern numbers can be obtained by $C = \gamma/2\pi$.

It is well known that the surface state exists at the boundary of photonic topological insulators with the different Berry phases. It is the inherent property of the photonic topological insulators. Next, we study the surface states supported by the interface between an arbitrary isotropic medium (ϵ, μ) and the gyroelectromagnetic metamaterial. The half-space $x > 0$ is occupied by the isotropic medium and the half-space $x < 0$ is the metamaterial. We use the method proposed by Dyakonov [46] to calculate the surface modes. According to the Maxwell's equations, the eigenfields on either side of the interface $(x = 0)$ are given by the nontrivial solutions of $\mathbf{E}$ and $\mathbf{H}$.

In the isotropic medium, the two orthogonal eigenmodes can be expressed as

$$\mathbf{E}_1 = \left(-k_y k_{x1}, \epsilon\mu\omega^2 - k_y^2, -k_y k_z\right), \quad \mathbf{H}_1 = (-\epsilon\omega k_z, 0, \epsilon\omega k_{x1}), \tag{4}$$

$$\mathbf{E}_2 = \left(k_z k_{x1}, k_y k_z, -\epsilon\mu\omega^2 + k_z^2\right), \quad \mathbf{H}_2 = (-\epsilon\omega k_y, \epsilon\omega k_{x1}, 0), \tag{5}$$

where $k_{x1} = \sqrt{\epsilon\mu\omega^2 - k_y^2 - k_z^2}$ is the normal direction wave vector. Similarly, two eigenstates of the gyroelectromagnetic metamaterial can be expressed as

$$\mathbf{E}_3 = \left(\frac{\omega\epsilon_t^{1.5}k_y + i(g\omega + k_z)k_x^+}{2g\omega k_z + k_z^2 + \omega^2\left(g^2 - \epsilon_t^2\right)}, \frac{ik_y(g\omega + k_z) - \omega\epsilon_t k_x^+}{2g\omega k_z + k_z^2 + \omega^2\left(g^2 - \epsilon_t^2\right)}, i\right), \tag{6}$$

$$\mathbf{H}_3 = \left(\frac{-i\omega\epsilon_t^{1.5}k_y + (g\omega + k_z)k_x^+}{2g\omega k_z + k_z^2 + \omega^2\left(g^2 - \epsilon_t^2\right)}, \frac{k_y(g\omega + k_z) + i\omega\epsilon_t k_x^+}{2g\omega k_z + k_z^2 + \omega^2\left(g^2 - \epsilon_t^2\right)}, 1\right), \tag{7}$$

$$\mathbf{E}_4 = \left(\frac{\omega\epsilon_t^{1.5}k_y + i(g\omega - k_z)k_x^-}{-2g\omega k_z + k_z^2 + \omega^2\left(g^2 - \epsilon_t^2\right)}, \frac{ik_y(g\omega - k_z) - \omega\epsilon_t k_x^-}{-2g\omega k_z + k_z^2 + \omega^2\left(g^2 - \epsilon_t^2\right)}, -i\right), \tag{8}$$

$$\mathbf{H}_4 = \left(\frac{i\omega\epsilon_t^{1.5}k_y + (-g\omega + k_z)k_x^-}{-2g\omega k_z + k_z^2 + \omega^2\left(g^2 - \epsilon_t^2\right)}, \frac{k_y(-g\omega + k_z) - i\omega\epsilon_t k_x^-}{-2g\omega k_z + k_z^2 + \omega^2\left(g^2 - \epsilon_t^2\right)}, 1\right), \tag{9}$$

where $k_x^\pm = -\sqrt{(-k_y^2\epsilon_t - (\pm 2\omega g k_z + k_z^2 + \omega^2(g^2 - \epsilon_t^2))\epsilon_z)/\epsilon_t}$.

The superscripts + and − refer to two independent polarizations in the metamaterial. The eigenfields in Eqs. (4)–(9) share the common tangential wave vector components k_y and k_z across the interface, as a direct consequence of the phase matching of electromagnetic fields.

The tangential components in Eqs. (4)–(9) are continuous across the interface, leading to the determinant problem of a 4×4 constraint matrix **M**,

$$\mathrm{Det}[\mathbf{M}] = \begin{vmatrix} E_{1y} & E_{2y} & E_{3y} & E_{4y} \\ E_{1z} & E_{2z} & E_{3z} & E_{4z} \\ H_{1y} & H_{2y} & H_{3y} & H_{4y} \\ H_{1z} & H_{2z} & H_{3z} & H_{4z} \end{vmatrix} = 0. \tag{10}$$

The characteristic equation of the surface modes are given as

$$\left(i\epsilon\omega^3\left(\epsilon k_{x1}^2 C_2 + C_3 + 2k_{x1}(C_4 + C_5 - ik_y\epsilon_t C_6)\right)\right)/C_1 = 0, \tag{11}$$

where the effective parameters are defined as

$$\begin{aligned}
C_1 &= \left(-2g\omega k_z + k_z^2 + \omega^2\left(g^2 - \epsilon_t^2\right)\right)\left(2g\omega k_z + k_z^2 + \omega^2\left(g^2 - \epsilon_t^2\right)\right), \\
C_2 &= -2igk_y\left(-k_z^2 + \omega^2\left(g^2 - \epsilon_t^2\right)\right) + C_7, \\
C_3 &= \mu\left(\epsilon\mu\omega^2 - k_y^2 - k_z^2\right)\left(-2igk_y\left(-k_z^2 + \omega^2\left(g^2 - \epsilon_t^2\right)\right) + C_7\right), \\
C_4 &= \epsilon\mu k_z^4 - k_z^2\left(2g^2\epsilon\mu\omega^2 + (2\epsilon\mu\omega^2 + k_x^+k_x^-)\epsilon_t^2\right) + \epsilon\mu\omega^2\left(g^4\omega^2 + (-2g^2\omega^2 + k_x^+k_x^-)\epsilon_t^2 + \omega^2\epsilon_t^4\right), \\
C_5 &= k_y^2\left((g^2 + \epsilon\mu)k_z^2 - \omega^2\left(g^4 + g^2\epsilon\mu - 2g^2\epsilon_t^2 + \epsilon_t^4\right)\right), \\
C_6 &= k_x^+\left(g\epsilon\mu\omega^2 + gk_z^2 - \omega k_z\left(g^2 + \epsilon\mu - \epsilon_t^2\right)\right) + k_x^-\left(g\epsilon\mu\omega^2 + gk_z^2 + \omega k_z\left(g^2 + \epsilon\mu - \epsilon_t^2\right)\right), \\
C_7 &= \epsilon_t\left(k_x^+\left(-2g\omega k_z + k_z^2 + \omega^2\left(g^2 - \epsilon_t^2\right)\right) + k_x^-\left(2g\omega k_z + k_z^2 + \omega^2\left(g^2 - \epsilon_t^2\right)\right)\right).
\end{aligned}$$

IV. GAPLESS PHOTONIC SURFACE WAVES IN THE COMMON BANDGAP REGION

Here, we assume an ideal situation that the overall material system has electromagnetic duality symmetry [35]. Figure 2(a) shows the surface states [based on Eq. (11)] at the interface between the vacuum ($\epsilon = \mu = 1$) and the gyroelectromagnetic metamaterial with $\overline{\boldsymbol{\mu}} = \overline{\boldsymbol{\epsilon}}$ ($\epsilon_t = 2, \epsilon_z = -2$, and $g = 0.5$). The surface states connect the vacuum (green solid line) to the bulk state (cyan line) of the metamaterial. The two surface states (LCP and RCP) do not interact owing to the electromagnetic duality symmetry of the system [35]. It should be noted that only the surface states in the common bandgap region have robust transmission. The Berry curvatures on the $k_x - k_y - \omega$ surfaces are shown in Figs. 2(b) and 2(c). The Berry curvatures are mainly concentrated near the center of the k space for the metamaterial. The Berry curvature is negligible when the wave vector increases to infinity. Based on Eq. (3), the Berry phases $\gamma = \pm 2\pi$ can be obtained. It corresponds to quantized Chern numbers of ±1 [see Fig. 2(a)].

As presented in Fig. 2(a), there are two surface states in the common bandgap region. The robust propagation property of the gapless surface states can be confirmed by numerical

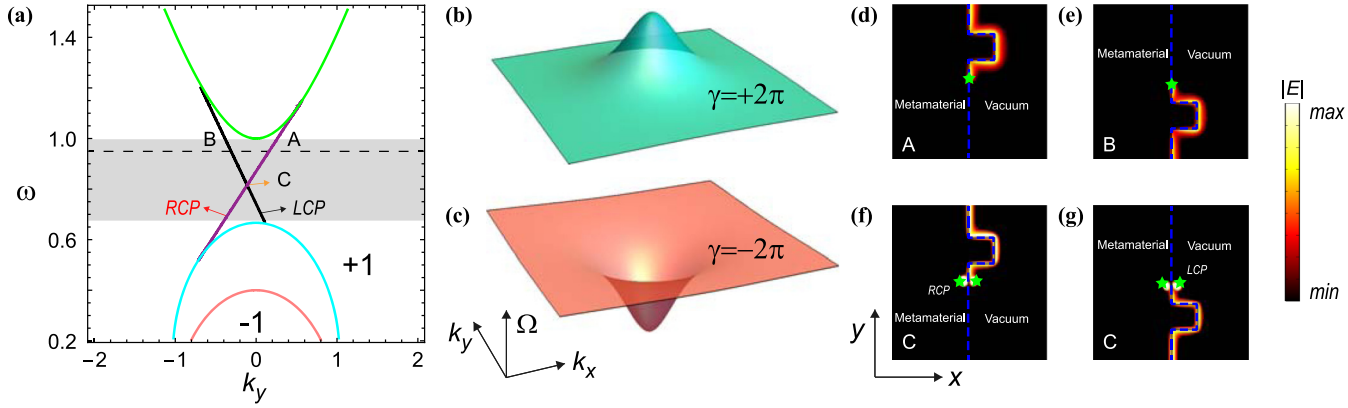

FIG. 2. Topological properties of the gyroelectromagnetic metamaterial. (a) The cyan/pink lines and the green solid line represent 2D band structures of the metamaterial and vacuum, respectively. The gray region corresponds to the common bandgap. The gapless surface states are colored with purple and black lines. The LCP (black lines) and RCP (purple lines) represent left and right circular polarizations on the vacuum side, respectively. The number label assigned to each bulk state represents its associated Chern number. (b) The distribution of the Berry curvature (Ω) of the cyan band in (a). (c) The distribution of the Berry curvature of the pink band in (a). (d) and (e) Simulation of the surface waves with $\omega = 0.95$, corresponding to points "A" and "B" in (a). (f) and (g) The field distributions of surface waves with $\omega = 0.815$ at the intersection point "C" in (a). The green pentagram represents the electric dipole. The parameters of the metamaterial are $\epsilon_t = 2$, $\epsilon_z = -2$, $g = 0.5$, and $k_z = 1$, respectively.

simulation (COMSOL multiphysics) at the interface (denoted by the blue dashed lines) between the metamaterial and the vacuum, as shown in Figs. 2(d)–2(g). A dipole source is placed at the interface to excite the surface waves, as depicted in Figs. 2(d) and 2(e). One corresponds to the positive y-direction transmission (point "A"). The other is in the negative y direction (point "B"). Owing to the opposite ellipticity, the two surface waves can propagate independently although they have the same frequency. The robust propagation indicates the nontrivial topological characteristics of the gyroelectromagnetic metamaterial system. Moreover, the degenerate state at point "C" can be regarded as the superposition of two orthogonal modes. These two orthogonal surface states can be distinguished by their opposite ellipticities. It is analog to the spin Hall effect in the electronic system [38]. We use two electric dipoles to excite the left and right circular polarized surface states at point "C," respectively. Figures 2(f) and 2(g) show the robust propagation of these two surface waves.

V. GAPPED PHOTONIC SURFACE STATES IN THE MATERIAL SYSTEM WITHOUT ELECTROMAGNETIC DUALITY SYMMETRY

In Fig. 3(a), we calculate the surface states on the interface ($x = 0$) between an isotropic medium with $\mu \neq \epsilon$ ($\mu = 1$ and $\epsilon = 1.2$) and the gyroelectromagnetic metamaterial with $\overline{\boldsymbol{\mu}} = \overline{\boldsymbol{\epsilon}}$ ($\epsilon_t = 2$, $\epsilon_z = -2$, and $g = 0.5$). Different from the case in Fig. 2(a), the isotropic medium has different relative permittivity and permeability. Thus, the electromagnetic duality symmetry of the material system is broken. The symmetry breaking lifts the degeneracy of the two surface states. A small gap of the surface states arises at $k_y = -0.13$. In this case, the surface states (red/black lines) are not spanning the whole bandgap. There is no surface state distribution in the orange region [Fig. 3(a)]. Hence, the gapped surface states arise when the electromagnetic duality symmetry of the material system is broken. It is worth noting that the asymmetry of material on either side of the interface can break the electromagnetic duality.

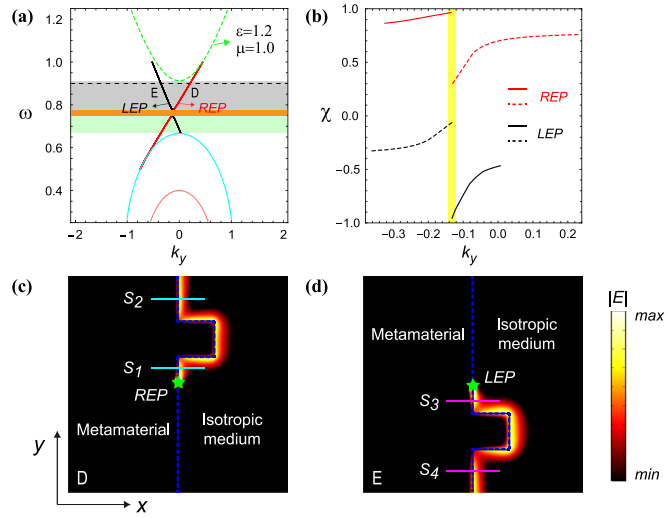

FIG. 3. Gapped surface states in the material system without electromagnetic duality symmetry. (a) The cyan/pink lines and the green dashed line represent 2D band structures of the metamaterial and the isotropic medium ($\mu = 1$ and $\epsilon = 1.2$), respectively. The gray and light green regions correspond to the bandgaps. The orange region is the gap of the surface states. The red and black curve lines are the gapped surface states. The LEP and REP represent left and right elliptical polarizations on the metamaterial side, respectively. (b) The dashed and solid lines represent the ellipticities of the gray and light green shadow areas in (a), respectively. (c) and (d) Simulation of propagation of the surface waves at points "D" and "E" in (a), respectively. $S_1(S_2)$ and $S_3(S_4)$ represent the energy flow of the surface waves before and after passing through the square defect, respectively. The electromagnetic parameters of the metamaterial are the same as in Fig. 2.

Starting from the boundary condition, the ellipticities of the surface state can be calculated following the steps below [35]. First, the electric field on the isotropic material and the gyroelectromagnetic metamaterial side can be obtained by summing the two independent eigenfields in Eqs. (4)–(9)

$$\mathbf{E}^{\mathrm{iso}} = (A_1\mathbf{E}_1 + A_2\mathbf{E}_2), \quad \mathbf{E}^{\mathrm{gyr}} = (A_3\mathbf{E}_3 + A_4\mathbf{E}_4), \qquad (12)$$

where A_1, A_2, A_3, and A_4 are constants. The polarization ellipticities of the surface state lie in a plane perpendicular to the interface because the energy flow is along the interface. The polarization ellipticities can then be calculated by the tangential and vertical components of the electric field at a point which is very close to the boundary. The electric field components in Eq. (12) are projected to the left ($C_{\mathrm{LCP}} = (E_x^{\mathrm{iso(gyr)}} + iE_t^{\mathrm{iso(gyr)}})/\sqrt{2}$) and right ($C_{\mathrm{RCP}} = (E_x^{\mathrm{iso(gyr)}} - iE_t^{\mathrm{iso(gyr)}})/\sqrt{2}$) circular polarization states, where $E_t^{\mathrm{iso(gyr)}}$ is the complex amplitude of the tangential electric field $(0, E_y^{\mathrm{iso(gyr)}}, E_z^{\mathrm{iso(gyr)}})^T$. Then, the ellipticities of the surface state can be obtained by $\chi = (|C_{\mathrm{RCP}}| - |C_{\mathrm{LCP}}|)/(|C_{\mathrm{RCP}}| + |C_{\mathrm{LCP}}|)$.

We calculate the ellipticities of the gapped surface states on the metamaterial side and show them in Fig. 3(b). First, the surface states are not pure circularly polarized modes when the electromagnetic duality is broken. Second, there is an obvious singularity at $k_y = -0.13$ where the ellipticity is uncertain. Near the singularity, the ellipticity changes drastically as illustrated by the yellow shade in Fig. 3(b). So, although the degeneracy is lifted as shown in the band diagram [Fig. 3(a)], the two surface states with different ellipticity cannot smoothly transform to each other. There is no smooth transition zone between them.

Apart from the singularity position, the two surface states can still robustly propagate without backscattering. For the gapped surface states, the robust propagation property can be confirmed at the interface between the metamaterial and the isotropic medium in Figs. 3(c) and 3(d). The transmissions of the gapped surface waves are given in Figs. 3(c) and 3(d), corresponding to points "D" and "E" ($\omega = 0.9$) in Fig. 3(a), respectively. To check the robustness of these surface waves, the square obstacles are inserted as defects. The surface waves can bypass the sharp corners and no scattering occurs [the ratios $S_2/S_1(S_4/S_3)$ approximately equal to 1].

VI. FILTERING EFFECT IN A PHOTONIC TOPOLOGICAL GYROELECTROMAGNETIC METAMATERIAL SYSTEM

In this paper, the surface wave filter consists of three parts: region I, region II, and region III, as shown in Fig. 4. For the regions I/III and II, the surface states are located on the interface between the vacuum/isotropic medium ($\mu \neq \epsilon$) and the gyroelectromagnetic metamaterial. It should be noted that region I is the same as region III, so they have the same band properties. The surface states in regions I/III and II are gapless [Fig. 2(a)] and gapped [Fig. 3(a)] types, respectively. The waves are incident from region I (port) and finally are transmitted into region III, as illustrated in Fig. 4.

Now we study the surface wave behaviors in the filter (Fig. 4). To show the results more clearly, we focus on the behavior of the right elliptical polarization surface state. The surface state with the same polarization can nearly freely pass through the filter. The gapless and gapped surface states exist in the regions I/III and the region II, respectively. The band diagrams and the transmission curves are depicted in Figs. 5(a) and 5(b), respectively. In particular, there exist two possible paths: transmitting to the region III or completely reflected back. Here and in the following, the transmission (T) is numerically calculated (COMSOL multiphysics) by the ratio of the energy flow of the surface wave in region III to the incident surface wave in region I (Fig. 4). The transmittance (T) approaches to 1 in the gray regions in Fig. 5(a). Namely, the surface waves from region I can be almost completely

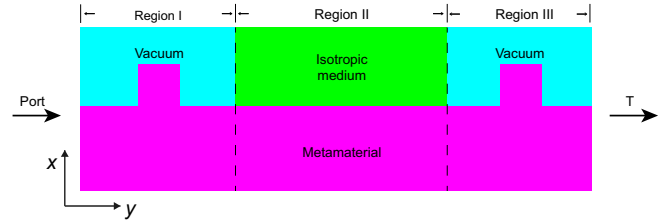

FIG. 4. Schematic diagram for the photonic filtering device. The device consists of regions I, II, and III. The cyan, green, and magenta regions represent the vacuum, isotropic medium, and metamaterial, respectively. T is the transmission of the surface waves through the photonic filtering device.

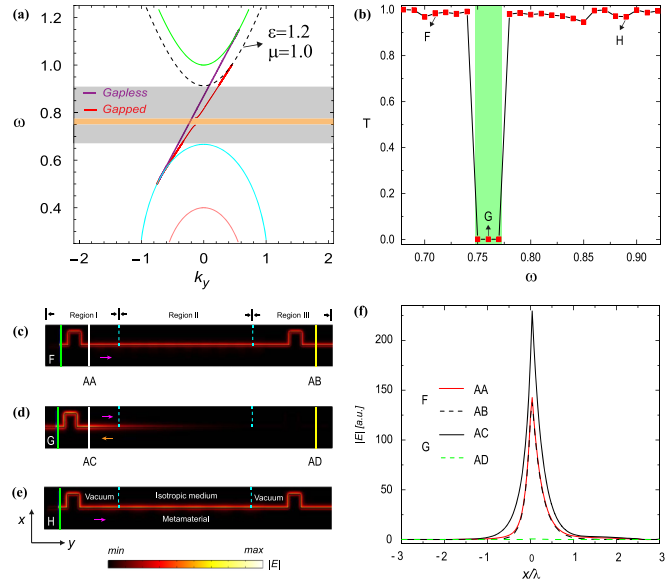

FIG. 5. Filtering effect. (a) The cyan/pink lines and the green solid/black dashed lines represent 2D band structures of the metamaterial and the vacuum/isotropic medium ($\mu = 1$ and $\epsilon = 1.2$), respectively. The purple and red curve lines are RCP gapless [Fig. 2(a)] and REP gapped [Fig. 3(a)] surface states, respectively. The gray regions correspond to the common bandgaps. The orange region is the gap of the surface states. (b) Transmission spectra (T) from region I to region III (Fig. 4). (c)–(e) Simulation of the propagation of the surface waves at points "F", "G", and "H" in (b), respectively. (f) One-dimensional field profiles, corresponding to points "F" and "G" at lines AA/AB and AC/AD in (c) and (d), respectively. The electromagnetic parameters of the metamaterial are the same as in Fig. 2.

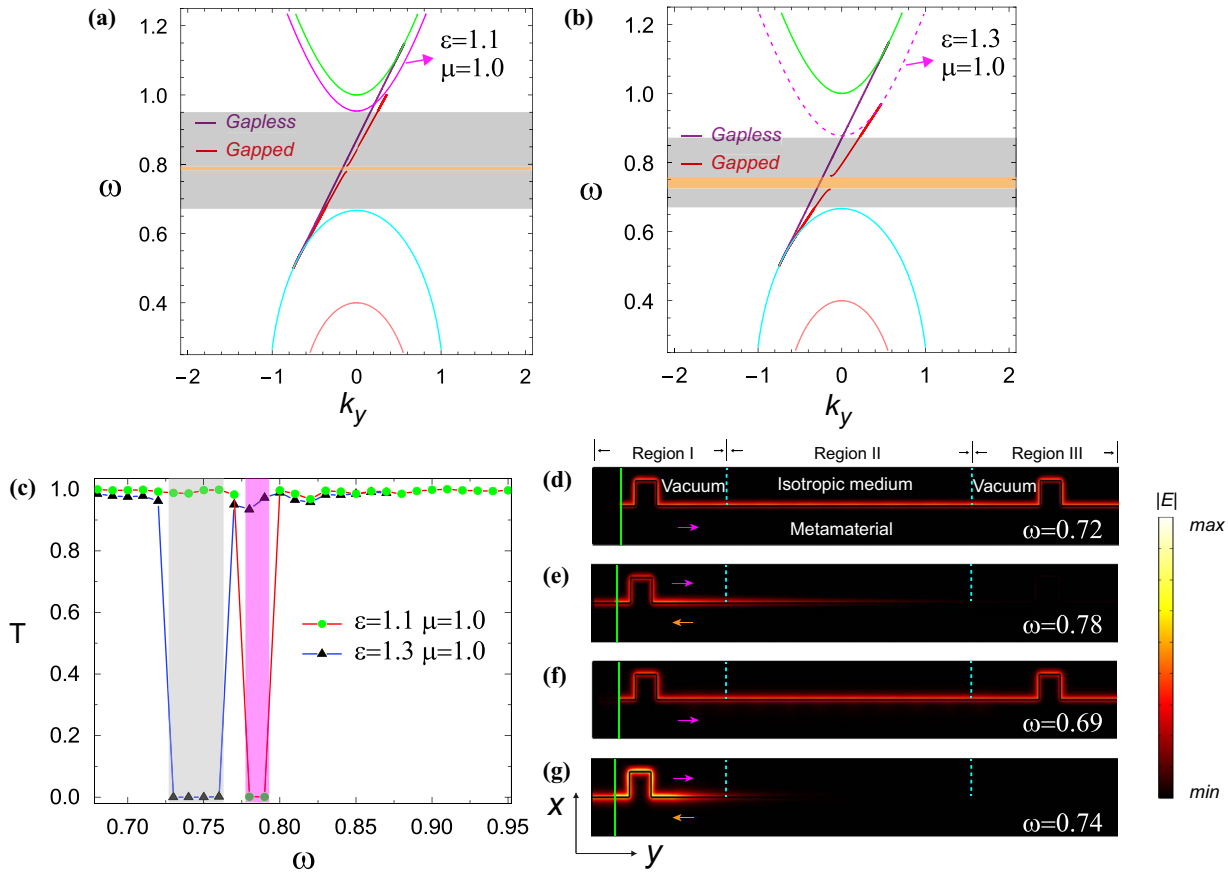

FIG. 6. Bandwidth-controllable filtering effect. (a) and (b) The cyan/pink lines and the green solid line represent 2D band structures of the metamaterial and the vacuum, respectively. The magenta solid and dashed lines represent 2D band structures of the isotropic medium $\mu = 1, \epsilon = 1.1$ and $\mu = 1, \epsilon = 1.3$, respectively. The gray regions correspond to the common bandgaps. The orange regions is the gap of the surface states. The purple and red curve lines are RCP gapless and REP gapped surface states, respectively. (c) Transmission spectra (T) from region I to region III (Fig. 4). (d) and (e) Simulation of the propagation of the surface waves at $\omega = 0.72$ and $\omega = 0.78$ of the isotropic medium ($\mu = 1$ and $\epsilon = 1.1$) in (c), respectively. (f) and (g) Simulation of the propagation of the surface waves at $\omega = 0.69$ and $\omega = 0.74$ of the isotropic medium ($\mu = 1$ and $\epsilon = 1.3$) in (c), respectively. The electromagnetic parameters of the metamaterial are the same as in Fig. 2.

transmitted to region III because of the topological properties of the metamaterial. On the other hand, the transmission drops rapidly to zero in the green region of Fig. 5(b). The origin of the filtering effect is that there is no surface mode in the region II of Fig. 4. The surface wave incident from region I is completely reflected back. Note that the orange region in Fig. 5(a) corresponds to the green region in Fig. 5(b). It directly verifies the theoretical analysis.

The transmission of the surface waves are given in Figs. 5(c)–5(e), corresponding to the points "F" ($\omega = 0.71$), "G" ($\omega = 0.76$), and "H" ($\omega = 0.89$) in Fig. 5(b). In Figs. 5(c) and 5(e), the surface waves from region I can be nearly fully transmitted to region III. However, the surface wave incident from region I is completely reflected back in Fig. 5(d). The profiles of the incident and the transmitted surface state are almost the same for point "F," as depicted in Fig. 5(f). However, for point "G," there is almost no field distributed in region III (green dashed line). The surface field is concentrated in region I (black solid line) due to the filtering effect, as shown in Fig. 5(f).

Figures 6(a) and 6(b) show the results of gapped surface states when the permittivity of the isotropic material is 1.1 and 1.3. The gaps of the surface states are located at $\omega \in [0.78, 0.79]$ and $\omega \in [0.73, 0.76]$, respectively. The transmittance of the surface waves through region II (Fig. 4) covered by these two materials are shown in Fig. 6(c). The transmission patterns of the surface waves are given in Figs. 6(d)–6(g), corresponding to $\omega = 0.72$, $\omega = 0.78$, $\omega = 0.69$, and $\omega = 0.74$ in Fig. 6(c), respectively. The surface waves from region I can be nearly fully transmitted to region III in Figs. 6(d) and 6(f). Figures 6(e) and 6(g) show the cases where the surface wave incident from region I is completely reflected back. Thus, by changing the electromagnetic parameters of isotropic materials, the filtering effect with controllable bandwidth can be realized.

VII. REALIZATION OF THE PROPOSED GYROELECTROMAGNETIC METAMATERIAL

In Fig. 7(a), we propose a periodic layered structure to realize the gyroelectromagnetic metamaterial. The bilayer superlattice is composed of a magnetized plasma layer [47] (magenta) with relative permeability μ_1 and a ferrimagnetic garnet layer [11] (yellow) with relative permittivity ϵ_2. More-

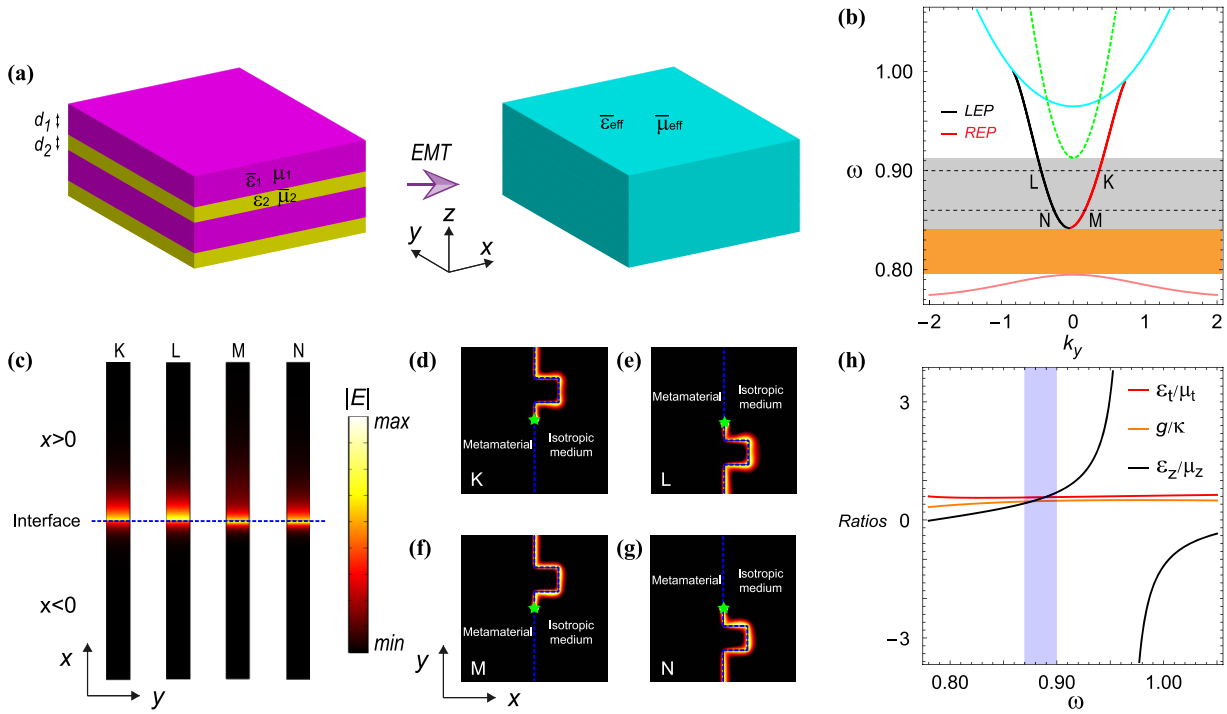

FIG. 7. (a) Illustration of the proposed gyroelectromagnetic metamaterial as a superlattice composed of a magnetized plasma layer and a ferrimagnetic garnet layer. The layers are infinite in the xy plane. (b) The cyan/pink lines and the green dashed line represent 2D band structures ($k_z = 1$) of the dispersive metamaterial and the isotropic medium ($\mu = 1$ and $\epsilon = 1.2$), respectively. (c) Mode profiles $|E|$ of the gapped surface states, corresponding to points "K", "L", "M," and "N" in (b), respectively. (d) and (e) Simulation of the robust surface waves at the interface between the isotropic medium and the metamaterial with $\omega = 0.9$, corresponding to points "K" and "L" in (b). (f) and (g) The field distributions of surface waves with $\omega = 0.86$ at points "M" and "N" in (b). The parameters of the magnetized plasma and ferrimagnetic garnet layers are $\omega_p = 1.625\omega_0$, $|\omega_B| = 0.325\omega_0$, $\mu_1 = 5$, $|\omega_m| = 0.9\omega_0$, and $\epsilon_2 = 7$, respectively. (h) The ratios of effective electromagnetic parameters of the proposed gyroelectromagnetic metamaterial.

over, the thicknesses of the magnetized plasma layer and the ferrimagnetic garnet layer are d_1 and d_2 ($d_1 = 2d_2$), respectively.

For the magnetized plasma layer, the relative permittivity tensor is

$$\bar{\boldsymbol{\epsilon}}_1 = \begin{pmatrix} \alpha & i\delta & 0 \\ -i\delta & \alpha & 0 \\ 0 & 0 & \beta \end{pmatrix}, \tag{13}$$

where $\alpha = 1 - \omega_p^2/(\omega^2 - \omega_B^2)$, $\delta = \omega_B\omega_p^2/(\omega(\omega^2 - \omega_B^2))$, and $\beta = 1 - \omega_p^2/\omega^2$. Here, ω is the angle frequency, ω_p represents the plasma frequency, and ω_B is the cyclotron frequency.

According to the effective medium theory (EMT) [28,48], the effective relative permittivity tensor of the metamaterial can be written as

$$\bar{\boldsymbol{\epsilon}}_{\text{eff}} = \begin{pmatrix} \frac{d_1\alpha + d_2\epsilon_2}{d_1 + d_2} & \frac{id_1\delta}{d_1 + d_2} & 0 \\ -\frac{id_1\delta}{d_1 + d_2} & \frac{d_1\alpha + d_2\epsilon_2}{d_1 + d_2} & 0 \\ 0 & 0 & \frac{(d_1 + d_2)\beta\epsilon_2}{d_1\epsilon_2 + d_2\beta} \end{pmatrix}. \tag{14}$$

For the ferrimagnetic garnet layer, the relative permeability tensor is

$$\bar{\boldsymbol{\mu}}_2 = \begin{pmatrix} \mu & i\sigma & 0 \\ -i\sigma & \mu & 0 \\ 0 & 0 & \mu \end{pmatrix}, \tag{15}$$

where $\mu = 1 + \omega_0\omega_m/(\omega_0^2 - \omega^2)$ and $\sigma = \omega\omega_m/(\omega^2 - \omega_0^2)$. Here, ω_0 represents the resonance frequency and ω_m is the characteristic frequency. The signs of ω_m and ω_B depend on the orientation of the extra magnetic field [11,47].

The effective relative permeability tensor of the metamaterial is given by

$$\bar{\boldsymbol{\mu}}_{\text{eff}} = \begin{pmatrix} \frac{d_1\mu_1 + d_2\mu}{d_1 + d_2} & \frac{id_2\sigma}{d_1 + d_2} & 0 \\ -\frac{id_2\sigma}{d_1 + d_2} & \frac{d_1\mu_1 + d_2\mu}{d_1 + d_2} & 0 \\ 0 & 0 & \frac{(d_1 + d_2)\mu\mu_1}{d_1\mu + d_2\mu_1} \end{pmatrix}. \tag{16}$$

The effective electromagnetic parameters are inevitably dispersive since the media of both layers in Fig. 7(a) have dispersions. In this case, the effective electromagnetic parameters of relative permittivity and permeability tensors of the gyroelectromagnetic metamaterial can be written as

$$\bar{\boldsymbol{\epsilon}}_{\text{eff}} = \begin{pmatrix} \epsilon_t & ig & 0 \\ -ig & \epsilon_t & 0 \\ 0 & 0 & \epsilon_z \end{pmatrix}, \quad \bar{\boldsymbol{\mu}}_{\text{eff}} = \begin{pmatrix} \mu_t & i\kappa & 0 \\ -i\kappa & \mu_t & 0 \\ 0 & 0 & \mu_z \end{pmatrix}, \tag{17}$$

where $\epsilon_t = (2(1 - \omega_p^2/(\omega^2 - \omega_B^2)) + \epsilon_2)/3$, $g = 2\omega_p^2\omega_B/(3\omega(\omega^2 - \omega_B^2))$, $\mu_t = (1 + \omega_0\omega_m/(-\omega^2 + \omega_0^2) + 2\mu_1)/3$, $\kappa = \omega\omega_m/(3(\omega^2 - \omega_0^2))$, $\epsilon_z = (3(1 - \omega_p^2/\omega^2)\epsilon_2)/(1 - \omega_p^2/\omega^2 + 2\epsilon_2)$, $\mu_z = 3\mu_1(1 + \omega_0\omega_m/(-\omega^2 + \omega_0^2))/(2(1 + \omega_0\omega_m/(-\omega^2 + \omega_0^2)) + \mu_1)$.

In Fig. 7(b), we plot the two-dimensional (2D) band structures and surface states on the dispersive gyroelectromagnetic metamaterial using the effective electromagnetic parameters in Eq. (17). Similar to Fig. 3(a), the isotropic medium with different relative permittivity and permeability ($\mu = 1$ and $\epsilon = 1.2$), so the gapped surface states also arise in Fig. 7(b). The gray region is the common bandgap. The orange region is the gap of the surface states. The gapped surface states are colored with red and black lines. The four points on the gapped surface states all have field localization, as shown in Fig. 7(c). The $x > 0$ and $x < 0$ regions are the isotropic medium and the metamaterial, respectively. The robust propagation property of the gapped surface states can be confirmed by numerical simulation at the interface, as shown in Figs. 7(d)–7(g). The surface waves can stably bypass the square defects. In particular, for the common bandgap region, the surface waves propagate along the positive y direction (points "K" and "M"). The others propagate along the negative y direction (points "L" and "N"). It is similar to the results in Figs. 3(c) and 3(d). Comparing Fig. 3 with Fig. 7, the bandgap width decreases owing to the effect of dispersion. However, the dispersion of the metamaterial does not change its main characteristics, i.e., the robustness of the surface waves. Previous studies have shown that the dispersion of the material has no decisive influence on the topological properties [10,12,40]. Thus, the dispersion of the metamaterial is not considered in Eq. (1) to simplify our theoretical analysis.

In general, the electromagnetic duality symmetry in the metamaterial is usually achieved by a fixed ratio between the permittivity and permeability tensor elements [35,49]. Here, we examine the electromagnetic duality symmetry of the proposed gyroelectromagnetic metamaterial [Fig. 7(a)]. The ratios of the effective electromagnetic parameters [Eq. (17)] for the metamaterial [Fig. 7(a)] are given in Fig. 7(h). The electromagnetic duality cannot be satisfied for all frequencies [Fig. 7(h)] due to the material dispersion [40]. However, the ratios of the permittivity and permeability tensor elements are roughly equal to each other in $\omega \in [0.87, 0.90]$, as shown by the light purple region in Fig. 7(h). In this case, the metamaterial can be regarded as having electromagnetic duality symmetry [36].

VIII. CONCLUSIONS

In conclusion, we have studied the photonic gapped surface states in the topological gyroelectromagnetic metamaterial. When the electromagnetic duality symmetry of the material system is broken, the gapped surface states arise. This kind of gapped surface wave can bypass the sharp corner, demonstrating its robust property. Moreover, the filtering effect occurs concomitantly in the gapped surface states. The square defects are considered along the interface of the filtering device to verify the robustness of our systems. The filtering effect with controllable bandwidth can be realized by changing the electromagnetic parameters of the isotropic materials.

ACKNOWLEDGMENTS

This work was supported by the National Natural Science Foundation of China (NSFC) (Grants No. 61575055, No. 11874132, and No. 12074087), and Fundamental Research Funds for the Central Universities (Grant No. 3072021CFT2501).

[1] L. Lu, J. D. Joannopoulos, and M. Soljačić,Topological photonics, Nat. Photon. **8**, 821 (2014).
[2] M. Kim, Z. Jacob, and J. Rho, Recent advances in 2D, 3D and higher-order topological photonics, Light-Sci. Appl. **9**, 130 (2020).
[3] A. B. Khanikaev and G. Shvets, Two-dimensional topological photonics, Nat. Photon. **11**, 763 (2017).
[4] M. G. Silveirinha, Quantized angular momentum in topological optical systems, Nat. Commun. **10**, 349 (2019).
[5] B. Xie, G. Su, H. Wang, H. Su, X. Shen, P. Zhan, M. Lu, Z. Wang, and Y. Chen, Visualization of Higher-Order Topological Insulating Phases in Two-Dimensional Dielectric Photonic Crystals, Phys. Rev. Lett. **122**, 233903 (2019).
[6] B. Yang, Y. G. Bi, R. X. Zhang, R. Y. Zhang, O. You, Z. H. Zhu, J. Feng, H. B. Sun, C. T. Chan, C. X. Liu, and S. Zhang, Momentum space toroidal moment in a photonic metamaterial, Nat. Commun. **12**, 1784 (2021).
[7] F. D. M. Haldane and S. Raghu, Possible Realization of Directional Optical Waveguides in Photonic Crystals with Broken Time-Reversal Symmetry, Phys. Rev. Lett. **100**, 013904 (2008).
[8] Z. Wang, Y. Chong, J. D. Joannopoulos, and M. Soljačić, Observation of unidirectional backscattering-immune topological electromagnetic states, Nature (London) **461**, 772 (2009).
[9] T. Ozawa, H. M. Price, A. Amo, N. Goldman, M. Hafezi, L. Lu, M. C. Rechtsman, D. Schuster, J. Simon, O. Zilberberg, and I. Carusotto, Topological photonics. Rev. Mod. Phys. **91**, 015006 (2019).
[10] Z. Wang, Y. D. Chong, J. D. Joannopoulos, and M. Soljačić, Reflection-Free One-Way Edge Modes in a Gyromagnetic Photonic Crystal, Phys. Rev. Lett. **100**, 013905 (2008).
[11] S. A. Skirlo, L. Lu, Y. Igarashi, Q. Yan, J. D. Joannopoulos, and M. Soljačić, Experimental Observation of Large Chern Numbers in Photonic Crystals, Phys. Rev. Lett. **115**, 253901 (2015).
[12] S. A. Skirlo, L. Lu, and M. Soljačić, Multimode One-Way Waveguides of Large Chern Numbers, Phys. Rev. Lett. **113**, 113904 (2014).
[13] W. Gao, M. Lawrence, B. Yang, F. Liu, F. Fang, B. Béri, J. Li, and S. Zhang, Topological Photonic Phase in Chiral Hyperbolic Metamaterials, Phys. Rev. Lett. **114**, 037402 (2015).
[14] R. C. Shiu, H. C. Chan, H. X. Wang, and G. Y. Guo, Photonic Chern insulators made of gyromagnetic hyperbolic metamaterials, Phys. Rev. Mater. **4**, 065202 (2020).
[15] J. Hou, Z. Li, X. Luo, Q. Gu, and C. Zhang, Topological Bands and Triply Degenerate Points in Non-Hermitian Hyperbolic Metamaterials, Phys. Rev. Lett. **124**, 073603 (2020).
[16] R. Chern and Y. Yu, Chiral surface waves on hyperbolic-gyromagnetic metamaterials, Opt. Express **25**, 11801 (2017).
[17] X. D. Chen, W. M. Deng, F. L. Zhao, and J. W. Dong, Accidental double Dirac cones and robust edge states in topological

anisotropic photonic crystals, Laser Photon. Rev. **12**, 1800073 (2018).

[18] M. L. Chen, L. J. Jiang, Z. H. Lan, and W. E. Sha, Coexistence of pseudospin- and valley-Hall-like edge states in a photonic crystal with C_{3v} symmetry, Phys. Rev. Res. **2**, 043148 (2020).

[19] Q. Chen, L. Zhang, S. Xu, Z. Wang, E. Li, Y. Yang, and H. Chen, Robust waveguiding in substrate-integrated topological photonic crystals, Appl. Rhys. Lett. **116**, 231106 (2020).

[20] L. Xu, H. Wang, Y. Xu, H. Chen, and J. Jiang, Accidental degeneracy in photonic bands and topological phase transitions in two-dimensional core-shell dielectric photonic crystals, Opt. Express **24**, 18059 (2016).

[21] M. I. Shalaev, S. Desnavi, W. Walasik, and N. M Litchinitser, Reconfigurable topological crystal, New J. Phys. **20**, 023040 (2018).

[22] J. Yang, X. Lü, C. Zhang, and H. Xie, Topological spin-valley filtering effects based on hybrid silicene-like nanoribbons, New J. Phys. **22**, 053034 (2020).

[23] J. Yang, X. Lü, and H. Xie, Current propagation behaviors and spin filtering effects in three-terminal topological-insulator junctions, New J. Phys. **22**, 103018 (2020).

[24] X. Li, C. Wang, M. Deng, H. Duan, P. Fu, R. Wang, L. Sheng, and D. Xing, Photo-Induced Weyl Half-Metal Phase and Spin Filter Effects from Topological Dirac Semimetals, Phys. Rev. Lett. **123**, 206601 (2019).

[25] X. Lü and H. Xie, Spin filters and switchers in topological-insulator junctions, Phys. Rev. Appl. **12**, 064040 (2019).

[26] H. Pan, X. Li, F. Zhang, and S. A. Yang, Perfect valley filter in a topological domain wall, Phys. Rev. B **92**, 041404(R) (2015).

[27] S. Cheng, R. Zhang, J. Zhou, H. Jiang, and Q. Sun, Perfect valley filter based on a topological phase in a disorder Sb monolayer heterostructure, Phys. Rev. B **97**, 085420 (2018).

[28] V. I. Fesenko and V. R. Tuz, Lossless and loss-induced topological transitions of isofrequency surface in a biaxial gyroeletromagnetic medium, Phys. Rev. B **99**, 094404 (2019).

[29] V. I. Fesenko, I. V. Fedorin, and V. R. Tuz, Dispersion regions overlapping for bulk and surface polaritons in a magnetic-semiconductor superlattice, Opt. Lett. **41**, 2093 (2016).

[30] M. G. Silveirinha, $P \cdot T \cdot D$ symmetry-protected scattering anomaly in optics, Phys. Rev. B **95**, 035153 (2017).

[31] V. R. Tuz, I. V. Fedorin, and V. I. Fesenko, Bi-hyperbolic isofrequency surface in a magnetic-semiconductor superlattice, Opt. Lett. **42**, 4561 (2017).

[32] V. R. Tuz, Polaritons dispersion in a composite ferrite-semiconductor structure near gyrotropic-nihility state, J. Magn. Mater. **419**, 559 (2016).

[33] N. Han, J. L. Liu, Y. Gao, K. Y. Zhou, and S. T. Liu, Topologically protected and highly localized surface waves in gyro-electromagnetic metamaterials, Ann. Phys. (Berlin) **532**, 2000022 (2020).

[34] I. F. Corbaton, X. Z. Puyalto, N. Tischler, X. Vidal, M. L. Juan, and G. M. Terriza, Electromagnetic Duality Symmetry and Helicity Conservation for the Macroscopic Maxwell's Equations, Phys. Rev. Lett. **111**, 060401 (2013).

[35] Q. Guo, B. Yang, L. Xia, W. Gao, H. Liu, J. Chen, Y. Xiang, and S. Zhang, Three Dimensional Photonic Dirac Points in Metamaterials, Phys. Rev. Lett. **119**, 213901 (2017).

[36] J. W. Dong, X. D. Chen, H. Zhu, Y. Wang, and X. Zhang, Valley photonic crystals for control of spin and topology, Nat. Mater. **16**, 298 (2017).

[37] A. Slobozhanyuk, S. H. Mousavi, X. Ni, D. Smirnova, Y. S. Kivshar, and A. B. Khanikaev, Three-dimensional all-dielectric photonic topological insulator, Nat. Photon. **11**, 130 (2017).

[38] Q. Guo, W. Gao, J. Chen, Y. Liu, and S. Zhang, Line Degeneracy and Strong Spin-Orbit Coupling of Light with Bulk Bianisotropic Metamaterials, Phys. Rev. Lett. **115**, 067402 (2015).

[39] D. J. Bisharat and D. F. Sievenpiper, Electromagnetic-dual metasurfaces for topological states along a 1D interface, Laser Photon. Rev. **13**, 1900126 (2019).

[40] A. B. Khanikaev, S. H. Mousavi, W. K. Tse, M. Kargarian, A. H. MacDonald, and G. Shvets, Photonic topological insulators, Nat. Mater. **12**, 233 (2013).

[41] Y. Kang, X. Ni, X. Cheng, A. B. Khanikaev, and A. Z. Genack, Pseudo-spin-valley coupled edge states in a photonic topological insulator, Nat. Commun. **9**, 2039 (2018).

[42] X. Cheng, C. Jouvaud, X. Ni, S. H. Mousavi, A. Z. Genack, and A. B. Khanikaev, Robust reconfigurable electromagnetic pathways within a photonic topological insulator, Nat. Mater. **15**, 542 (2016).

[43] C. He, X. C. Sun, X. P. Liu, M. H. Lu, Y. Chen, L. Feng, and Y. F. Chen, Photonic topological insulator with broken time-reversal symmetry, Proc. Natl. Acad. Sci. USA **113**, 4924 (2016).

[44] Y. Yang, Z. Gao, H. Xue, L. Zhang, M. He, Z. Yang, R. Singh, Y. D. Chong, B. L. Zhang, and H. Chen, Realization of a three-dimensional photonic topological insulator, Nature (London) **565**, 622 (2019).

[45] S. A. R. Horsley and M. Woolley, Zero-refractive-index materials and topological photonics, Nat. Phys. **17**, 348 (2021).

[46] M. I. Dyakonov, New type of electromagnetic wave propagating at the interface, Sov. Phys. JETP **67**, 714 (1998).

[47] S. Zhang, Y. Xiong, G. Bartal, X. Yin, and X. Zhang, Magnetized Plasma for Reconfigurable Subdiffraction Imaging, Phys. Rev. Lett. **106**, 243901 (2011).

[48] D. P. Tsai, B. Wood, and J. B. Pendry, Directed subwavelength imaging using a layered metal-dielectric system, Phys. Rev. B **74**, 115116 (2006).

[49] Q. Guo, O. You, B. Yang, J. Sellman, E. Blythe, H. Liu, Y. Xinag, D. Fan, J. Chen, C. T. Chan, and S. Zhang, Observation of Three-Dimensional Photonic Dirac Points and Spin-Polarized Surface Arcs, Phys. Rev. Lett. **122**, 203903 (2019).